Supporting Information

Identification of Single-Atom Active Sites in CO Oxidation Over Oxide-Supported Au Catalysts

Christian Schilling[1†], Marc Ziemba[1†], Christian Hess[1*], M. Verónica Ganduglia-Pirovano[2*]

[1]Eduard-Zintl-Institut für Anorganische und Physikalische Chemie, Technische Universität Darmstadt, Alarich-Weiss-Str. 8, 64287 Darmstadt, Germany

[2]Instituto de Catálisis y Petroleoquímica-Consejo Superior de Investigaciones Científicas, Marie Curie 2, 28049 Madrid, Spain

[†]Both authors contributed equally

Table of Contents

Experimental and Theoretical Methods

Experimental - Synthesis and Characterization

For details on the synthesis and characterization of CeO_2 and Au/CeO_2 samples please refer to our previous publications.[1-5] Briefly, ceria nanoparticles were prepared by decomposition of $Ce(NO_3)_3 \cdot 6\ H_2O$ (99.5 %, Alfa Aesar) at 600°C for two periods of 12 h. The ceria nanoparticles possess a termination in (111) direction as evident from transmission electron microcopy data and *in situ* Raman spectra. Thus the experimental results are directly comparable to those of the DFT calculations employing (111)-oriented ceria slabs. Au/CeO_2 samples with 0.5 wt% Au loading were synthesized via deposition precipitation from $HAuCl_4 \cdot 3\ H_2O$ (> 99.99 %, Sigma Aldrich).

Experimental - Operando Spectroscopy

Operando diffuse reflectance infrared Fourier transform spectroscopy (DRIFTS) was done at a Vertex 70 (Bruker) equipped with a liquid nitrogen cooled mercury cadmium telluride MCT detector operating at a resolution of 1 cm^{-1}. A commercial reaction cell (Praying Mantis™ High Temperature Reaction Chamber, Harrick Scientific Products) with infrared transparent CaF_2 windows was employed.[1]

Potassium Bromide (KBr) powder outgassed at 200°C for 1 h and cooled to room temperature was used as infrared transparent sample for the I_0 spectrum. The sample holder (stainless steel with a diameter of 8 mm and depth of 0.5 mm) covers about 30 mg of CeO_2 or Au/CeO_2 sample. A thermocouple in direct proximity to the sample revealed a temperature increase of 2°C during room temperature CO oxidation (21°C ± 2°C). Due to the minor temperature increase from the exothermal reaction, thermal effects at the sample can be safely ruled out.

The gas feed is composed of CO (99.997 %, Air Liquid), O_2 (99.999%, Westfalen), and Ar (99.996 % Westfalen). The gas stream from the reaction cell is analyzed by infrared

spectroscopy (FTIR, Tensor 20, Bruker) and the conversion is determined as the amount of CO_2 in the gas stream in relation to 2% CO in the inlet gas stream mixed by digital mass flow meters. Infrared spectra of the catalyst sample and of the gas stream are synchronized and saved every minute, providing an average over one minute.

The catalyst is either equilibrated in 25% O_2 (100 ml/min) for 1 h at room temperature (pretreatment A) or heated to 200°C in 25% O_2 for 1 h and then cooled to room temperature (pretreatment B). After the pretreatment the catalyst is exposed to reaction conditions (2% CO, 10% O_2 balanced with Ar to 100 ml/min) and to regenerating condition (25 % O_2). The exposure to reaction conditions and regenerating conditions is repeated once more.

Density Functional Theory Calculations

Spin-polarized Density Functional Theory (DFT) calculations were carried out employing the VASP package (version 5.3.5 https://www.vasp.at)[6-9] with the projector augmented wave (PAW) method[10] and the PBE functional,[11] with an additional Hubbard *U*-like potential applied to the Ce 4*f* orbitals[12] of U_{eff} = 4.5 eV (PBE+U/4.5 eV),[13,14] as well as the hybrid-DFT approach, using the HSE06 functional.[15-17] The CeO_2(111) surface with both (2 × 2) and (3 × 3) periodicities was modeled using a supercell approach containing a three O–Ce–O trilayer-thick slab with the previously (PBE+U/4.5 eV and HSE06) calculated ceria bulk lattice constants,[4] separated by at least a 10 Å-thick vacuum layer to avoid interactions between the surfaces. The Brillouin zone of the supercells with (2 × 2) and (3 × 3) surface periodicity was sample with (3 × 3 × 1) and (2 × 2 × 1) Γ-centered Monkhorst Pack[18] *k*-point grids for PBE+U/4.5 eV, and (2 × 2 × 1) and (1 × 1 × 1) grids for HSE06 calculations, respectively. Moreover, we modeled the interaction of individual Au_1 atoms and pyramidal Au_4 clusters on the CeO_2(111) surface. For the former, several adsorption sites have been explored, and the for the latter, a structure similar to the one reported to be most stable was used.[19] The adsorption energy of Au species is referenced to gas-phase Au atoms for which Γ-point only calculations were performed in a 15×15×15 $Å^3$ box. Furthermore, the adsorption of the Au_1 and Au_4 species on the reduced CeO_{2-x}(111) surface with one surface oxygen vacancy was also considered. For the Au_1 adsorption in the vacant site, different configurations for the excess charge have been considered, whereas for the Au_4 cluster, only one (see the DFT Results section below).

The energy cutoff was set to 400 eV. All of the atoms in the three bottom atomic layers were fixed at their optimized bulk-truncated positions during geometry optimization, whereas the rest of the atoms were allowed to fully relax. The maximum residual forces in the slabs were smaller than 0.01 eV/Å and the total energy was converged to 10^{-6} eV in the electronic SCF

loops. To account for dispersion interaction within the PBE+U/4.5 eV framework the DFT-D2 method of Grimme[20,21] was employed with semi-empirical parameters optimized before.[22] The adsorption energy of CO molecules is referenced to gas-phase CO for which Γ-point only calculations were performed in a 15×15×15 $Å^3$ box. The vibrational frequency of adsorbed CO was calculated after fixing all but the CO molecule by analytical calculation of the Hessian matrix using density functional perturbation theory[23,24] (PBE+U/4.5 eV) or a finite differences approach (PBE+U/4.5 eV + D2 and HSE06). Due to the localized character of the C–O vibration, the exclusion of the rest of the atoms in the supercell from the calculation of vibrational properties, changes the C–O vibrational frequency by < 0.1 cm^{-1}, as described before.[2] The SCF convergence criterion was set to 10^{-8} eV for the displaced structures during the finite differences calculations. For the calculation of the vibrational frequency of systems with ^{13}CO, a modified PAW potential for C was used, in which the atomic mass had been modified.

Supplementary Figures and Tables

Experimental Results

The analysis of the carbonyl region (2000 – 2300 cm^{-1}) is described in detail in the manuscript (MS). Please note that isotope experiments, which we performed by using ^{13}CO, rule out the presence of an electronic transition of reduced ceria discussed previously in the literature in the context of the water–gas shift reaction.[25] This can be justified by a complete shift of the bands in the CO region, which in turn results in the same signature (see Figure S1).

Based on the literature assignments,[26-29] the bands in the carbonate region (800 – 1800 cm^{-1}) in Figure 4 are assigned as follows: The bands at 988 cm^{-1}, 1298 cm^{-1}, and 1575 cm^{-1} are assigned to carbonate species; besides, the bands at 1050 cm^{-1}, 1254 cm^{-1}, 1358 cm^{-1}, and 1550 cm^{-1} are assigned to formate species, which are also stable on the ceria support after outgassing at 200°C. Under reaction conditions, bands at 1023 cm^{-1}, 1218 cm^{-1}, 1393 cm^{-1}, and 1620 cm^{-1} grow in intensity, and in the same way, the ν(OH) stretching mode at 3619 cm^{-1} [27] also grows in intensity. An isotopic exchange with ^{13}CO under reaction conditions (see Figure S2) strengthens the assignment of the bands. In addition, the observed shifts agree well with those obtained by DFT calculations. Focusing on the hydrogen carbonate bands, it can be seen that the isotopic exchange has no effect on the position of the bands at 1023 cm^{-1} and 1218 cm^{-1}. This behavior meets the expectations based on the nature of the vibrations [ν(CO_3, s) and δ(OCOH, as)]. Also, DFT calculations using ^{13}C show the same results (see Table S2). The situation is different for the bands at 1393 cm^{-1} and 1620 cm^{-1}. These bands show a significant shift, which is again consistent with the nature of the vibrations [ν(OCO, s) and ν(OCO, as)] and DFT calculations using ^{13}C (see Table S2). Hence, the bands at 1023 cm^{-1}, 1218 cm^{-1}, 1393 cm^{-1}, and 1620 cm^{-1} are assigned to hydrogen carbonate species adsorbed on the ceria support.

The band at 1218 cm^{-1}, which is assigned to a δ(OCOH) bending mode in hydrogen carbonate species, is most pronounced under reaction conditions after outgassing of the sample at 200°C.

As it does not overlap (see Figure 3 in the MS) with other bands, it can be evaluated quantitatively in a straightforward manner (see Figure 5 in the MS).

The carbonyl region (2000 – 2300 cm^{-1}) is shown enlarged in Figure 2 in the MS and is discussed in detail in the text.

The broad band between 3000 and 3500 cm^{-1} in Figure S3 is assigned to water adsorbed at the catalyst samples. The amount of adsorbed water is considerably lowered after outgassing of the sample at 200°C. Moreover, the band at 3694 cm^{-1} in Figure S4 can be assigned to the ν(OH) of adsorbed water.[27] Furthermore, the bands at 3730 and 3660 cm^{-1} in Figure S4 are assigned to hydroxyl stretching modes ν(OH-I) and ν(OH-II), i.e., hydroxyl coordinated to one or two Ce^{4+} ions [27] that shift slightly upon exposure to reaction conditions.[1]

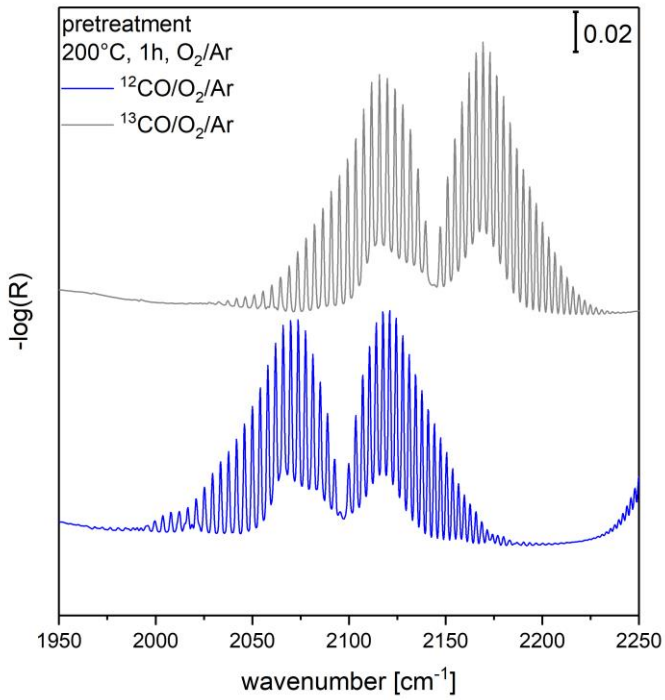

Figure S1: *Operando* diffuse reflectance infrared spectra (CO region) of a 0.5 wt% Au/CeO_2 catalyst after 1h at 200°C in 25% O_2 (pretreatment B) followed by reaction conditions with ^{12}CO (grey) and with ^{13}CO (blue). The spectra were recorded after ~30 minutes under reaction conditions. The spectrum under reaction conditions with ^{12}CO (grey) is offset for clarity.

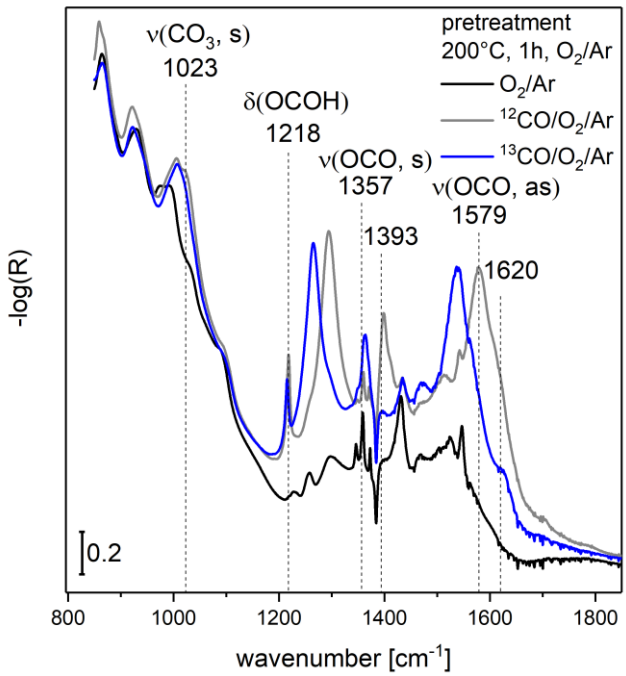

Figure S2: *Operando* diffuse reflectance infrared spectra (carbonate region) of a 0.5 wt% Au/CeO_2 catalyst in 25% O_2 at 21°C recorded directly after 1h at 200°C in 25% O_2 (pretreatment B, black) and after ~30 minutes in reaction conditions with ^{12}CO (grey) and with ^{13}CO (blue).

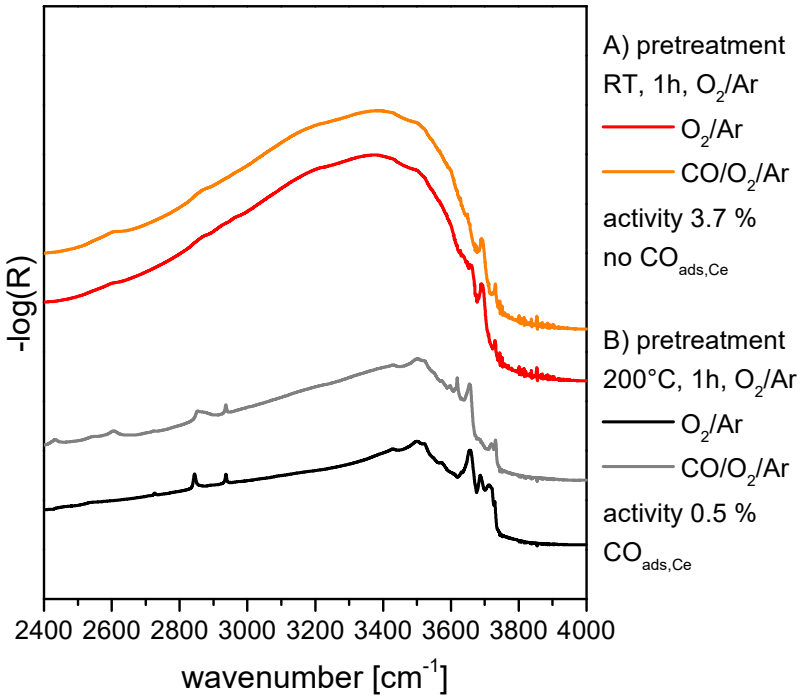

Figure S3: *Operando* diffuse reflectance infrared spectra (region of adsorbed water) of a 0.5 wt% Au/CeO_2 catalyst in 25% O_2 at 21°C recorded directly after equilibration in 25% O_2 (pretreatment A, red) and after ~30 minutes in reaction conditions (2% CO, 10% O_2, orange) and directly after 1h at 200°C in 25% O_2 (pretreatment B, black) and after ~30 minutes in reaction conditions (grey). The spectra are offset for clarity.

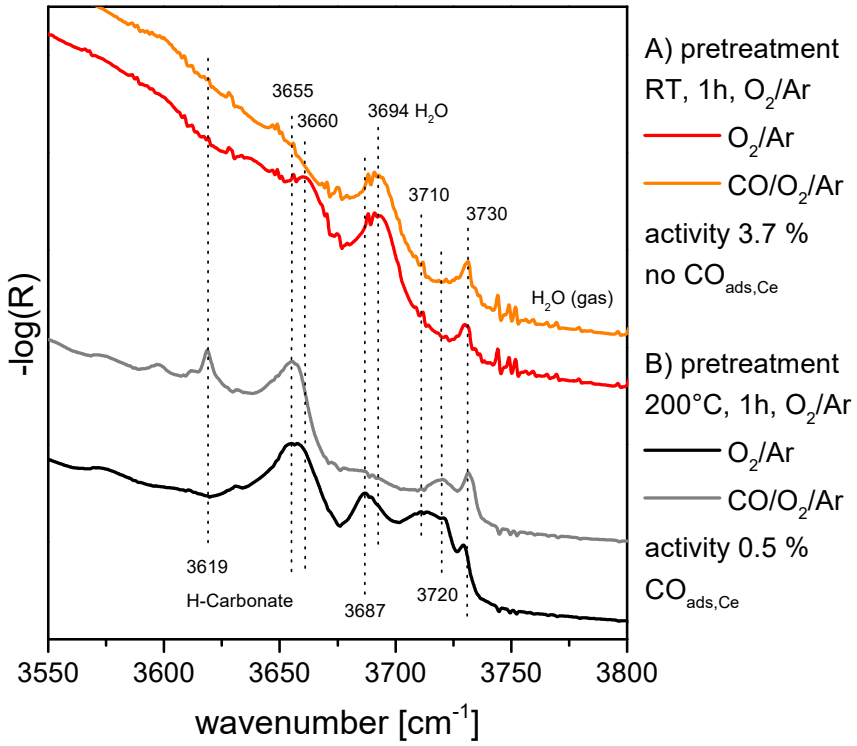

Figure S4: *Operando* diffuse reflectance infrared spectra (hydroxyl region) of a 0.5 wt% Au/CeO_2 catalyst in 25% O_2 at 21°C recorded directly after equilibration in 25% O_2 (pretreatment A, red) and after ~30 minutes in reaction conditions (2% CO, 10% O_2, orange) and directly after 1h at 200°C in 25% O_2 (pretreatment B, black) and after ~30 minutes in reaction conditions (grey). The spectra are offset for clarity.

Density Functional Theory Results

Within the PBE+U/4.5 eV framework, upon adsorption of a Au atom on the $CeO_2(111)$ surface [$Au_1/CeO_2(111)$], the transfer of the Au $6s^1$ electron to the support is predicted, which is accompanied by the formation of a Ce^{3+} ion, and thus the oxidation state of Au is 1+ (Au^+).[30-32] Two different adsorption structures are identified, namely, Au^+ adsorption on-top of a surface oxygen atom (Au@O, Figure 3C and D in the MS) and at a bridge position between two surface oxygen atoms (O-O bridge, Figure 3G and H). For both structures, the Au → ceria transferred charge can be localized either in nearest (NN) or next nearest neighbor cationic positions (NNN) to the gold ion. The PBE+U calculated Au adsorption energies, $E_{ads,Au}$ (Table S1), namely, $E_{ads,Au}$ = –0.966 eV (Au@O, Ce^{3+} NN), –1.017 eV (Au@O, Ce^{3+} NNN), –1.061 eV (Au@O-O bridge, Ce^{3+} NN), and –1.209 eV (Au@O-O bridge, Ce^{3+} NNN) show that for both sites (on-top O and O-O bridge), the Ce^{3+} NNN configurations are more stable than Ce^{3+} NN ones and that the most stable structure is the Au@O-O bridge with Ce^{3+} in a NNN site. The calculated $E_{ads,Au}$ values for the Au@O and Au@O-O bridge structures with Ce^{3+} localization in NNN sites can be compared to those in the literature (Au@O, $E_{ads,Au}$ = –1.04 eV and Au@O-O bridge, –1.18 eV[33], Au@O, –1.07 eV and Au@O-O bridge, –1.20 eV[30]), showing excellent consistency.

For comparison and validation, the calculations for the $Au_1/CeO_2(111)$ system were repeated with the HSE06 functional. With this functional, two stable Au@O structures are found, one in which no charge is transferred from gold to the surface [$Au_1^0/CeO_2(111)$] (see Figure 3E in the MS) with $E_{ads,Au}$ = –0.483 eV, in agreement with the literature,[32] and another one in which gold is positively charged (Au^+) and the Ce^{3+} is located in a NNN position (Figure 3D) with $E_{ads,Au}$ = –0.503 eV. A gold atom adsorbed at the Ce-Ce bridge position (Figure 3F) was also found not to transfer an electron to the surface,[31] and the adsorption energy for this structure is calculated as $E_{ads,Au}$ =–0.531 eV.[31] However, charge transfer is predicted for adsorption at the

O-O bridge position (Au^+). The configuration in which Ce^{3+} is located in a NN position is less stable ($E_{ads,Au}$ = –0.437 eV[31,33,34]) than that in which it is located in a NNN position ($E_{ads,Au}$ = –0.587 eV). As obtained with the PBE+U/4.5 eV functional, with the HSE06 one, the adsorption at the O-O bridge position with Ce^{3+} in a NNN position is also the most stable $Au_1/CeO_2(111)$ structure, although the other ones are close in energy within a 0.15 eV energy range. These $Au_1/CeO_2(111)$ structures are considered as starting point for the adsorption of CO, as described in the manuscript.

In the following, we briefly report on the adsorption of Au_1 atoms and pyramidal Au_4 clusters on the reduced $CeO_{2-x}(111)$ surface with a surface oxygen vacancy and two Ce^{3+} ions in NNN sites. For Au_1, only the adsorption into the defect has been reported (Au@vac),[35,36] which is accompanied by the formation of Au^- species and the $Ce^{3+} \rightarrow Ce^{4+}$ oxidation of one of the initially reduced cations [$Au_1/CeO_{2-x}(111)$]. We note that the formation of such a structure has been found to be kinetically hindered.[37] The structures of Au@vac considered are represented in Figure 3K in the MS (Ce^{3+} in a NN position) and L (Ce^{3+} in a NNN position) for which the adsorption energies of Au^- are $E_{ads,Au}$ = –2.196 and –2.439 eV (PBE+U/4.5 eV), respectively. In the case of the adsorption of a pyramidal Au_4 cluster on the reduced support [$Au_4/CeO_{2-x}(111)$], one of the atoms of the base detaches as Au^+ to then fill the vacant oxygen site (Figure 3Q in the MS) and thus changing its oxidation state from Au^+ to Au^-. We note that if we consider the adsorption of the pyramidal Au_4 cluster on the non-defective $CeO_2(111)$ surface [$Au_4/CeO_2(111)$] (Figure 3M), the formation of a surface vacancy with subsequent filling by a detached Au atom from the Au_4 cluster, does not modify the degree of reduction of the oxide support, which still entails the presence of two Ce^3.

The $Au_1/CeO_{2-x}(111)$ and $Au_4CeO_{2-x}(111)$ structures enable the calculation of the reaction energies, ΔE_0, for the CO oxidation by a lattice oxygen atom (Mars-van-Krevelen reaction mechanism) over the (most stable) $Au_1/CeO_2(111)$ and $Au_4/CeO_2(111)$ model catalysts as (cf.

Table S1):

$$CO\text{-}Au_1/CeO_2(111) \rightarrow Au/CeO_{2-x}(111) + CO_2^{gas} \qquad \Delta E_0 = +0.284 \text{ eV}$$

$$CO\text{-}Au_4/CeO_2(111) \rightarrow Au_4/CeO_{2-x}(111) + CO_2^{gas} \qquad \Delta E_0 = +0.512 \text{ eV}$$

The (PBE+U/4.5 eV) calculated reaction energy for the $Au_1/CeO_2(111)$ system is by ~0.3 eV larger than that previously reported (–0.02 eV)[38]. For a system with a larger Au_{20} gold cluster on ceria surface, a value of 0.49 eV has been reported,[36] which is in line with our calculated value for Au_4.

For a thorough analysis of the C–O bond stretching vibrational frequency ($\tilde{\nu}_{CO}$) of CO adsorbed on the $Au/CeO_2(111)$ model systems, the isolated CO molecule is studied first aiming at benchmarking. Therefore, similar parameters to those employed by Yang *et al.*[39] (U = 5 eV) are used here to model the isolated CO molecule on the ceria surface, including vdW contributions following the approach of Grimme[20,21] (DFT-D2) and the PBE+U/4.5 eV functional. A finite-difference approach with four displacements for each coordinate (NFREE = 4, VASP input) is used for calculating $\tilde{\nu}_{CO}^{gas}$. Our calculated C–O bond stretch frequency is $\tilde{\nu}_{CO}^{gas}$ =2122.0 cm^{-1}, which compares well to that reported by Yang *et al.*[39] (2122.5 cm^{-1}). For the calculations of the vibrational frequency of CO adsorbed on the $Au/CeO_2(111)$ model systems, only two displacements for each coordinate are considered (NFREE = 2). Reducing the number of displacements in the calculation of the Hessian matrix, results in $\tilde{\nu}_{CO}^{gas}$ = 2124.5 cm^{-1} (including vdW contributions) and 2121.9 cm^{-1} (neglecting vdW contributions), cf. Table S1. Generally, the inclusion of vdW contributions results in frequencies shifts of 0–4 cm^{-1}. Therefore, vdW contributions are only considered for CO adsorption on the $CeO_2(111)$ surface and on the $Au_1/CeO_2(111)$ structures (see Table S1).

The CO stretch frequency for CO adsorbed on an isolated Au in the gas phase resembles that of CO adsorbed on the top site of the Au_4 pyramid on $CeO_2(111)$ [cf. 2068.8/2197.5 and 2069.2/2199.4 cm^{-1}, respectively (PBE+U/4.5 eV/HSE06)]. Generally, redshifts with respect to

the gas-phase CO molecule [2121.9/2235.7 cm^{-1} (PBE/HSE06)], $\Delta\tilde{\nu}_{CO,gas}$, are considerably smaller with the HSE06 functional than with PBE. For example, for the CO-Au_4/CeO_2(111) with CO@Au_{top}, $\Delta\tilde{\nu}_{CO,gas}$ = –36.3 and –53.1 cm^{-1} with the HSE06 and PBE+U/4.5 eV, respectively.

A summary of all calculated frequencies is given in Table S1. An excerpt is shown in Table 1 of the manuscript together with the experimental results. All considered model structures are shown in Figure 3 of the MS.

Table S1: Total energy E_{tot} (PBE+U/4.5 eV, PBE+U/4.5 eV+D2, and HSE06 functionals), gold (Au_x^y) oxidation state (y), Au adsorption energy $E_{ads,Au}$ at the CeO_2(111) surface, adsorption energy E_{ads} for CO and hydrogen carbonate, and CO stretch frequency. All structures have a (2 × 2) periodicity with the exception of the Au_4/CeO_2(111) structures, which have a (3 × 3) periodicity. Please note that the table continuous on the next pages.

Structure	**Method**	E_{tot} **[eV]**	$E_{ads,Au}$ **[eV]**	E_{ads}^* **[eV]**	$\tilde{\nu}_{CO}$ **[cm^{-1}]**
CeO_2(111) [vacuum layer 24 Å hereinafter]	PBE+U	–291.330			
	PBE+U+D2	–295.480			
	HSE06	–382.006			
CO/CeO_2(111) Figure 3A	PBE+U	–306.321		–0.185	2126.2
	PBE+U+D2	–310.567		–0.281	2129.5
	HSE06	–400.382		–0.150	2250.7
CO_3H/CeO_{2-x}(111) Ce^{3+} NNN Figure 3B	PBE+U	–319.353		–1.655*	
CeO_2(111) [vacuum layer 36 Å hereinafter]	PBE+U	–291.318			
	PBE+U+D2	–295.467			
	HSE06	–381.990			

$Au_1/CeO_2(111)$	PBE+U	–292.469	–0.966		
Au@O Ce^{3+} NN	PBE+U+D2	–296.822	–1.170		
Figure 3C					
$Au_1/CeO_2(111)$	PBE+U	–292.520	–1.017		
Au@O Ce^{3+} NNN	PBE+U+D2	–296.882	–1.230		
Figure 3D	HSE06	–383.014	–0.503		
$Au_1/CeO_2(111)$	HSE06	–382.994	–0.483		
Au@O no Ce^{3+}					
Figure 3E					
$Au_1/CeO_2(111)$	PBE+U	unstable			
Au@Ce-Ce bridge	PBE+U+D2	unstable			
Figure 3F	HSE06	–383.042	–0.531		
$Au_1/CeO_2(111)$	PBE+U	–292.564	–1.061		
Au@O-O bridge	PBE+U+D2	–296.903	–1.251		
Ce^{3+} NN	HSE06	–382.948	–0.437		
Figure 3G					
$Au_1/CeO_2(111)$	PBE+U	–292.712	–1.209		
Au@O-O bridge	PBE+U+D2	–297.038	–1.386		
Ce^{3+} NNN	HSE06	–383.098	–0.587		
Figure 3H					
$CO\text{-}Au_1/CeO_2(111)$	PBE+U	–309.924		–2.406	2094.6
Au@O-O bridge	PBE+U+D2	–314.305		–2.461	2094.5
Ce^{3+} NN	HSE06	–403.623		–2.299	2219.4
$CO\text{-}Au_1/CeO_2(111)$	PBE+U	–310.023		–2.505	2091.5
Au@O-O bridge	PBE+U+D2	–314.399		–2.555	2094.2
Ce^{3+} NNN	HSE06	–403.752		–2.428	2217.2
$CeO_{2-x}(111)$	PBE+U	–284.126			
surf O_{vac} ; Ce^{3+} NNN					
$Au_1/CeO_{2-x}(111)$	PBE+U	–286.507	–2.196		
$Au^{-}@O_{vac}$,					
Ce^{3+} NN					

$Au_1/CeO_{2-x}(111)$ $Au^{-}@O_{vac}$, Ce^{3+} NNN	PBE+U	–286.750	–2.439		
$Au_4/CeO_2(111)$ [vacuum layer 36 Å hereinafter]	PBE+U HSE06	–665.390 –869.467			
CO-$Au_4/CeO_2(111)$ $CO@Au_{top}$ Figure 3N	PBE+U HSE06	–681.118 –888.461		–0.922 –0.768	2069.2 2199.4
CO-$Au_4/CeO_2(111)$ $CO@Au_{bottom,1}$ Figure 3O	PBE+U HSE06	–681.562 –888.950		–1.366 –1.257	2086.3 2214.7
CO-$Au_4/CeO_2(111)$ $CO@Au_{bottom,2}$ Figure 3P	PBE+U HSE06	–681.593 –888.982		–1.397 –1.289	2085.5 2213.9
$Au_4/CeO_{2-x}(111)$ Figure 3Q	PBE+U	–658.092			
Structure gas-phase	**Method**	E_{tot} **[eV]**	$E_{ads,Au}$ **[eV]**	$E_{ads,CO}$ **[eV]**	$\tilde{\nu}_{CO}$ **[cm^{-1}]**
Au_1	PBE PBE+D2 HSE06	–0.185 –0.185 –0.521			
CO-Au_1	PBE HSE06	–15.803 –18.700		–0.812 –0.407	2068.8 2197.5
CO	PBE PBE+D2 HSE06	–14.806 –14.806 –18.226			2121.9 2124.5 2235.7
CO_2	PBE06	–22.989			
H_2	PBE	–6.760			

Table S2: Calculated frequencies and assignments for the vibrations of the hydrogen carbonate (CO_3H/CeO_{2-x}(111) Ce^{3+} NNN, see Figure 3B) with ^{13}C und ^{12}C.

Structure	**Methods**	**Frequency [cm^{-1}]**	***Assignment***
$^{13}CO_3H/CeO_{2-x}$(111)	PBE+U	1566.3	ν(OCO, as)
Ce^{3+} NNN		1360.1	ν(OCO, s)
		1177.6	δ(OCOH)
		1004.4	ν(CO_3, s)
$^{12}CO_3H/CeO_{2-x}$(111)	PBE+U	1608.0	ν(OCO, as)
Ce^{3+} NNN		1395.8	ν(OCO, s)
Figure 3B		1177.2	δ(OCOH)
		1007.9	ν(CO_3, s)

Table S3. Bader charges (ΔQ, in |*e*|) of Au atoms in $Au_1/CeO_2(111)$ and of those of the $Au_4/CeO_2(111)$ system in contact with the support (base) and at apex of the Au_4 pyramid (top), as well as Bader charges of those Au atoms directly bonded to CO, upon CO adsorption.

Structure	ΔQ (base)	ΔQ (top)
$Au_1/CeO_2(111)$ Au@O-O bridge Ce^{3+} NNN		+0.35
CO-$Au_1/CeO_2(111)$ Au@O-O bridge Ce^{3+} NN		+0.55
CO-$Au_1/CeO_2(111)$ Au@O-O bridge Ce^{3+} NNN		+0.52
$Au_4/CeO_2(111)$	+0.22, +0.22, +0.25	–0.05
CO-$Au_4/CeO_2(111)$ CO@Au_{top}	+0.19, +0.18, +0.21	+0.16
CO-$Au_4/CeO_2(111)$ CO@$Au_{bottom,1}$	+0.20, +0.55, +0,17	–0.11
CO-$Au_4/CeO_2(111)$ CO@$Au_{bottom,2}$	+0.19, +0.18, +0.54	–0.11

References

1. Schilling, C.; Hess, C. CO Oxidation on Ceria Supported Gold Catalysts Studied by Combined Operando Raman/UV–Vis and IR Spectroscopy. *Top. Catal.* **2017**, *60*, 131-140.
2. Filtschew, A.; Hofmann, K.; Hess, C. Ceria and Its Defect Structure: New Insights From a Combined Spectroscopic Approach. *J. Phys. Chem. C* **2016**, *120*, 6694-6703.
3. Schilling, C.; Hofmann, A.; Hess, C.; Ganduglia-Pirovano, M. V. Raman Spectra of Polycrystalline CeO_2: A Density Functional Theory Study. *J. Phys. Chem. C* **2017**, *121*, 20834-20849.
4. Schilling, C.; Ganduglia-Pirovano, M. V.; Hess, C. Experimental and Theoretical Study on the Nature of Adsorbed Oxygen Species on Shaped Ceria Nanoparticles. *J. Phys. Chem. Lett.* **2018**, *9*, 6593-6598.
5. Schilling, C.; Hess, C. Real-Time Observation of the Defect Dynamics in Working Au/CeO_2 Catalysts by Combined Operando Raman/UV-Vis Spectroscopy. *J. Phys. Chem. C* **2018**, *122*, 2909-2917.
6. Kresse, G.; Hafner, J. Ab Initio Molecular Dynamics for Liquid Metals. *Phys. Rev. B* **1993**, *47*, 558-561.
7. Kresse, G.; Hafner, J. Ab Initio Molecular-Dynamics Simulation of the Liquid-Metal-Amorphous-Semiconductor Transition in Germanium. *Phys. Rev. B* **1994**, *49*, 14251-14269.
8. Kresse, G.; Furthmüller, J. Efficiency of Ab-Initio Total Energy Calculations for Metals and Semiconductors Using a Plane-Wave Basis Set. *Comput. Mater. Sci.* **1996**, *6*, 15-50.
9. Kresse, G.; Furthmüller, J. Efficient Iterative Schemes for *Ab Initio* Total-Energy Calculations Using a Plane-Wave Basis Set. *Phys. Rev. B* **1996**, *54*, 11169-11186.
10. Kresse, G.; Joubert, D. From Ultrasoft Pseudopotentials to the Projector Augmented-Wave Method. *Phys. Rev. B* **1999**, *59*, 1758-1775.
11. Perdew, J. P.; Burke, K.; Ernzerhof, M. Generalized Gradient Approximation Made Simple. *Phys. Rev. Lett.* **1996**, *77*, 3865-3868.
12. Dudarev, S. L.; Botton, G. A.; Savrasov, S. Y.; Humphreys, C. J.; Sutton, A. P. Electron-Energy-Loss Spectra and the Structural Stability of Nickel Oxide: An LSDA+U Study. *Phys. Rev. B* **1998**, *57*, 1505-1509.

13. Ganduglia-Pirovano, M. V.; Hofmann, A.; Sauer, J. Oxygen Vacancies in Transition Metal and Rare Earth Oxides: Current State of Understanding and Remaining Challenges. *Surf. Sci. Rep.* **2007**, *62*, 219-270.
14. Fabris, S.; de Gironcoli, S.; Baroni, S.; Vicario, G.; Balducci, G. Taming Multiple Valency With Density Functionals: A Case Study of Defective Ceria. *Phys. Rev. B* **2005,** *71*, 041102.
15. Krukau, A. V.; Vydrov, O. A.; Izmaylov, A. F.; Scuseria, G. E. Influence of the Exchange Screening Parameter on the Performance of Screened Hybrid Functionals. *J. Chem. Phys.* **2006**, *125*, 224106.
16. Heyd, J.; Scuseria, G. E.; Ernzerhof, M. Hybrid Functionals Based on a Screened Coulomb Potential. *J. Chem. Phys.* **2003**, *118*, 8207-8215.
17. Heyd, J.; Scuseria, G. E.; Ernzerhof, M. Erratum: "Hybrid Functionals Based on a Screened Coulomb Potential". *J. Chem. Phys.* **2006**, *124*, 219906.
18. Monkhorst, H. J.; Pack, J. D. Special Points for Brillouin-Zone Integrations. *Phys. Rev. B* **1976**, *13*, 5188-5192.
19. Teng, B.-T.; Wu, F.-M.; Huang, W.-X.; Wen, X.-D.; Zhao, L.-H.; Luo, M.-F. A DFT Study of the Structures of Au_x Clusters on a CeO_2(111) Surface. *ChemPhysChem* **2012**, *13*, 1261-1271.
20. Grimme, S. Accurate Description of Van Der Waals Complexes by Density Functional Theory Including Empirical Corrections. *J. Comput. Chem.* **2004**, *25*, 1463-1473.
21. Grimme, S. Semiempirical GGA-Type Density Functional Constructed With a Long-Range Dispersion Correction. *J. Comput. Chem.* **2006**, *27*, 1787-1799.
22. Tosoni, S.; Boese, A. D.; Sauer, J. Interaction Between Gold Atoms and Thio-Aryl Ligands on the Au(111) Surface. *J. Phys. Chem. C* **2011**, *115*, 24871-24879.
23. Baroni, S.; de Gironcoli, S.; Dal Corso, A.; Giannozzi, P. Phonons and Related Crystal Properties From Density-Functional Perturbation Theory. *Rev. Mod. Phys.* **2001**, *73*, 515-562.
24. Gajdoš, M.; Hummer, K.; Kresse, G.; Furthmüller, J.; Bechstedt, F. Linear Optical Properties in the Projector-Augmented Wave Methodology. *Phys. Rev. B* **2006**, 73, 045112.
25. Daly, H.; Ni, J.; Thompsett, D.; Meunier, F.C. On the Usefulness of Carbon Isotopic Exchange for the Operando Analysis of Metal-Carbonyl Bands by IR Over Ceria-Containing Catalysts. *J. Catal.* **2008**, *254*, 238-243.

26. Vayssilov, G. N.; Mihaylov, M.; Petkov, P. S.; Hadjiivanov, K. I.; Neyman, K. M. Reassignment of the Vibrational Spectra of Carbonates, Formates, and Related Surface Species on Ceria: A Combined Density Functional and Infrared Spectroscopy Investigation. *J. Phys. Chem. C* **2011**, *115*, 23435-23454.
27. Binet, C.; Daturi, M.; Lavalley, J.-C. IR Study of Polycrystalline Ceria Properties in Oxidised and Reduced States. *Catal. Today* **1999**, *50*, 207-225.
28. Li, C.; Sakata, Y.; Arai, T.; Domen, K.; Maruya, K.-I.; Onishi, T. Carbon Monoxide and Carbon Dioxide Adsorption on Cerium Oxide Studied by Fourier-Transform Infrared Spectroscopy. Part 1.-Formation of Carbonate Species on Dehydroxylated CeO_2, at Room Temperature. *J. Chem. Soc., Faraday Trans. 1* **1989**, *85*, 929-943.
29. Li, C.; Sakata, Y.; Arai, T.; Domen, K.; Maruya, K.-I.; Onishi, T. Adsorption of Carbon Monoxide and Carbon Dioxide on Cerium Oxide Studied by Fourier-Transform Infrared Spectroscopy. Part 2.-Formation of Formate Species on Partially Reduced CeO_2 at Room Temperature. *J. Chem. Soc., Faraday Trans. 1* **1989**, *85*, 1451-1461.
30. Zhang, C.; Michaelides, A.; King, D. A.; Jenkins, S. J. Structure of Gold Atoms on Stoichiometric and Defective Ceria Surfaces. *J. Chem. Phys.* **2008,** *129*, 194708.
31. Penschke, C.; Paier, J. Reduction and Oxidation of Au Adatoms on the CeO_2(111) Surface - DFT+*U Versus* Hybrid Functionals. *Phys. Chem. Chem. Phys.* **2017**, *19*, 12546-12558.
32. Hernandez, N. C.; Grau-Crespo, R.; de Leeuw, N. H.; Sanz, J. F. Electronic Charge Transfer Between Ceria Surfaces and Gold Adatoms: a GGA+U Investigation. *Phys. Chem. Chem. Phys.* **2009**, *11*, 5246-5252.
33. Pan, Y.; Nilius, N.; Freund, H.-J.; Paier, J.; Penschke, C.; Sauer, J. Titration of Ce^{3+} Ions in the CeO_2(111) Surface by Au Adatoms. *Phys. Rev. Lett.* **2013**, *111*, 206101.
34. Kósmider, K.; Brázdová, V.; Ganduglia-Pirovano, M. V.; Pérez, R. Do Au Atoms Titrate Ce^{3+} Ions at the CeO_{2-x}(111) Surface? *J. Phys. Chem. C* **2016**, *120*, 927-933.
35. Camellone, M. F.; Fabris, S. Reaction Mechanisms for the CO Oxidation on Au/CeO_2 Catalysts: Activity of Substitutional Au^{3+}/Au^{+} Cations and Deactivation of Supported Au^{+} Adatoms. *J. Am. Chem. Soc.* **2009**, *131*, 10473-10483.
36. Wang, Y.-G.; Mei, D.; Glezakou, V.-A.; Li, J.; Rousseau, R. Dynamic Formation of Single-Atom Catalytic Active Sites on Ceria-Supported Gold Nanoparticles. *Nat. Commun.* **2015,** *6*, 6511.
37. Lustemberg, P. G. *et al.* Diffusion Barriers Block Defect Occupation on Reduced CeO_2(111). *Phys. Rev. Lett.* **2016**, *116*, 236101.

38. Ghosh, P.; Camellone, M. F.; Fabris, S. Fluxionality of Au Clusters at Ceria Surfaces During CO Oxidation: Relationships Among Reactivity, Size, Cohesion, and Surface Defects From DFT Simulations. *J. Phys. Chem. Lett.* **2013**, *4*, 2256-2263.

39. Yang, C. *et al.* Chemical Activity of Oxygen Vacancies on Ceria: a Combined Experimental and Theoretical Study on CeO_2(111). *Phys. Chem. Chem. Phys.* **2014**, *16*, 24165-24168.